This is the Preprint Version.

WILEY-VCH

High-power and ultrastable aqueous calcium-ion batteries enabled by small organic molecular crystal anodes

*Renjie Li, Jingya Yu, Feiyang Chen, K.C. Chan, Zheng-Long Xu**

Renjie Li, Jingya Yu, Feiyang Chen, Prof. K.C. Chan, Dr. Zheng-Long Xu
Department of Industrial and Systems Engineering, The Hong Kong Polytechnic University, Hung Hom, Hong Kong SAR, China.
E-mail: zhenglong.xu@polyu.edu.hk

Dr. Zheng-Long Xu
State Key Laboratory of Ultra-precision Machining Technology, The Hong Kong Polytechnic University, Hung Hom, Hong Kong, SAR, China.

Dr. Zheng-Long Xu
Research Institute of Advanced Manufacturing, The Hong Kong Polytechnic University, Hung Hom, Hong Kong SAR, China.

Keywords: Ca-ion batteries, organic electrodes, PTCDI, aqueous electrolyte

Calcium ion batteries (CIBs) have been pursued as potentially low-cost and safe alternatives to current Li-ion batteries due to the high abundance of calcium element. However, the large and divalent nature of Ca^{2+} leads to strong interaction with intercalation hosts, sluggish ion diffusion kinetics and low power output. Here, we report a small molecular organic anode, tetracarboxylic diimide (PTCDI), involving carbonyl enolization (C=O↔C-O^-) in aqueous electrolytes, which bypasses the diffusion difficulties in intercalation-type electrodes and avoid capacity sacrifice for polymer organic electrodes, thus manifesting rapid and high Ca storage capacities. In an aqueous Ca-ion cell, the PTCDI presents a reversible capacity of 112 mAh g^{-1}, a high capacity retention of 80 % after 1000 cycles and a high-power capability at 5 A g^{-1}, which rival the state-of-the-art anode materials in CIBs. Experiments and simulations reveal that Ca ions are diffusing along the *a* axis tunnel to enolize carbonyl groups without being entrapped in the

aromatic carbon layers. The feasibility of PTCDI anodes in practical CIBs is demonstrated by coupling with cost-effective Prussian blue analogous cathodes and $CaCl_2$ aqueous electrolyte. The appreciable Ca storage performance of small molecular crystals would spur the development of green organic CIBs.

1. Introduction

Lithium-ion batteries (LIBs) have gained great success in powering electric vehicles and portable electronics in the past decades. The rapidly growing demands of electrochemical energy storage systems for the growing smart grid and electrified transportation applications have raised concerns on raw material supply, given the limited and unevenly distributed lithium resources.[1] On the path of exploring new battery chemistries with improved sustainability and affordability, multivalent ion batteries are regarded promising. The potentially doubled or tripled capacities from multivalent ion insertion have stimulated tremendous efforts.[2] However, their intrinsically large polarities and ionic sizes induce sluggish ion diffusion kinetics in electrolytes and electrodes, consequently leading to low capacity utilizations.[3] The ionic potential is defined as the ratio of the charge number over the ion radius.[4] Among the representative multivalent ions (*i.e.*, Ca^{2+}, Mg^{2+}, Zn^{2+}, and Al^{3+}), the relatively large Ca^{2+} exhibits the smallest polarization strength, suggesting faster Ca^{2+} migration kinetics.[5] In addition, on the standard hydrogen electrode scale, the Ca/Ca^{2+} delivers the lowest reduction potential of -2.9 V for potentially high voltage and high energy Ca-ion batteries (CIBs). Together with the environmental benignity and high abundance (4.1% in the Earth's crust) of calcium element, CIB is considered a promising post-Li battery technology.

The implementation of CIBs has been hindered by the lack of suitable electrode materials.[6] For nonaqueous CIBs, Ca metal with the highest specific capacity (1335 mAh g^{-1}) and the lowest reduction potential among all possible anode materials were demonstrated irreversible in aprotic electrolytes.[7] Although several recently reported electrolytes claimed

reversible Ca metal stripping/plating, the unstable solid electrolyte interphase (SEI) and low coulombic efficiencies suppressed their viabilities.[8] Other anode materials, like Sn, Si and graphite,[9] also suffered kinetic difficulties and poor cyclabilities during alloying or intercalation reactions.[10] Regarding to the cathode materials, metal oxides, Prussian blue analogs and phosphates can indicate appreciable Ca ion storage capacities.[11] Nevertheless, few cathodes could deliver reasonable capacities at high current densities in nonaqueous electrolytes. Above obstacles are rooted on the divalent nature of Ca^{2+}, which intrinsically deteriorates the ion dissociation in electrolytes and solid-state-ion diffusion in host materials that the two essential processes in classic intercalation chemistry. To circumvent these issues, aqueous calcium-ion batteries (ACIBs) using organic electrode materials are desirable due to the fast ion diffusion kinetics in aqueous electrolytes and the rapid enolization chemistry in flexible organic frameworks.[9] The nonflammability of ACIBs further appeal their energy storage applications.[12]

However, unlike transition metal oxide electrodes, organic electrode materials are held together by weak van der Waals forces between molecules. They are often vulnerable to dissolve in aqueous electrolytes, resulting in material degradation, shuttle effect of intermediates and eventually poor cycling stability.[13] Effective polymerization could mitigate the dissolution problem but the introduction of inactive groups in long chain polymers would sacrifice the specific capacities. Moreover, it is not trivial to manipulate the polymerization procedures with appreciable product yielding. The capacity surrendering issue of organic electrodes could be tackled by selecting robust small molecular crystals. The strong crystal structures with inter-molecular H-bonding can restrain the integrity of active materials in aqueous electrolytes. Some small organics are abundantly found in nature with low cost and simple processing procedures. To this end, several aromatic carbonyl materials have been reported in CIBs with incentive electrochemical properties.[14] Nevertheless, deep understandings of the Ca storage mechanisms in high-performance small organic crystals have

yet been approached.

In this work, we proposed the perylene tetra-carboxylic diimide (PTCDI) as a new anode material in long-cycling and high-power ACIBs. The PTCDI material with robust chemical structure demonstrates a high reversible capacity of 112 mAh g^{-1}, a record-high capacity retention of 80% over 1000 cycles, and remarkable rate capability at 5 A g^{-1} in 1 M $CaCl_2 \cdot 2H_2O$ aqueous electrolyte. The Ca ion storage mechanisms are elucidated by a suit of non-trivial characterizations like *in-situ* X-ray diffraction (XRD), ^{13}C nuclear magnetic resonance (NMR), electrochemical quartz crystal microbalance (EQCM), and theoretical calculations. It is revealed that the reversible enolization redox process (O=C↔C-O^-) of PTCDI with one dimensional Ca^{2+} diffusion pathways as well as the absence of covalent bond cleavage or reformation offer the basis for notable reversibility and high-rate capability. We also demonstrate the feasibility of the PTCDI in Ca ion full cells by paring with Prussian blue analogue (PAB) cathodes. The new ACIBs delivered a high energy density of 64.5 Wh kg^{-1} at a cycling power of 1000 W kg^{-1}, which ravels the state-of-the-art CIBs.

2. Results and discussion

Several organic molecules containing different numbers of aromatic rings and redox motifs have been demonstrated feasible in storing Ca in aqueous electrolytes, such as polyimide poly[N,N-(ethane-1,2-diyl)-1,4,5,8-naphthalenetetracarboxiimide] (PNDIE), 5,7,12,14-pentacenetetrone (PT), poly(anthraquinonyl sulfide) (PAQs), and 3,4,9,10-perylene tetracarboxylic dianhydride (PTCDA).[14] Despite their reasonable capacities (approximate 100 mAh g^{-1}), the complicated synthesize procedures for PNDIE and PAQs polymers, the partial dissolution of calciated PTCDA, and the high-cost for PT crystals offset their sustainability and competitiveness for CIBs. PTCDI is a well-known source of vat dyes and pigments with wide applications in dye-sensitized solar cells, transistors and biological photovoltaics. PTCDI presents a high carbonyl group concentration and moderate-sized aromatic rings, therefore it

attracted our immediate attention for Ca ion storage. The morphology and structure of as-received PDCTI are illustrated in **Figure 1**. Figure 1a shows the Retiled refinement of XRD pattern that indicates a pure and high-crystalline structure with a monoclinic *P21/n* space group. The high crystallinity of PTCDI is different from the major amorphous organic electrode materials in literature.[15] The refined lattice parameters and crystallographic information are tabulated in **Table S1** and **S2**. The PTCDI can be schematically described as uniformly aligned and packed wave-layer crystals (Figure 1b).

The PTCDI powder exhibits a prismatic morphology with average particle sizes of 500 nm as illustrated in scanning electron microscopy (SEM) (Figure 1c) and transmission electron microscopy (TEM) images (Figure 1d). The selected area electron diffraction (SAED) patterns of an individual PTCDI nanorod (Figure 1d) exhibits a sharp lattice fringe of $(13\,\bar{1})$, corresponding to the *d*-spacing of 0.277 nm, which is consistent with the XRD result. Figure 1e shows the Fourier transform infrared (FTIR) spectrum of PTCDI with strong adsorption peaks at 1682 and 1668 cm^{-1}, referring to the stretching vibration of carbonyl groups. The adsorption peak at approximately 1572 cm^{-1} could be assigned to the stretching vibration of C=C in the aromatic ring. The C–N bonds are indicated by the stretching peaks at 1360 and 1273 cm^{-1}.

To evaluate the electrochemical property of PTCDI in ACIBs, cyclic voltammetry (CV) profiles (**Figure 2a**) were recorded at a scan rate of 0.2 mV s^{-1} using a three-electrode configuration in 1 M $CaCl_2 \cdot 2H_2O$ aqueous solution. The initial cycling profile presents cathodic and anodic peaks at -0.7 V and -0.5/-0.16 V *vs.* Ag/AgCl, corresponding to the Ca ion storing and releasing behaviors, respectively. From the 2nd cycle and forward, the cathodic peak was positively shifted to -0.56 V *vs.* Ag/AgCl and retained intact, possibly due to the activation of molecular crystals at the initial calciation.[16] The overlapped CV curves from the 2nd to 4th cycles suggest excellent reversibility of the electrochemical system. When cycling at a low current density of 0.1 A g^{-1}, the PTCDI anode could deliver a discharge capacity of 160 mAh g^{-1} and a moderate coulombic efficiency of 70.1%. The initially irreversible capacity can be

attributed to side reactions like hydrogen evolution reaction in dilute aqueous electrolyte. [17] The reversible capacity is 112 mAh g^{-1}, indicating an 81% utilization of its theoretical capacity of 137 mAh g^{-1} by calculating a two-electron transfer of each carbonyl group in PTCDI.

The rate capability of PTCDI was investigated by galvanostatic charging–discharging at increasing rates as shown in Figure 2b. When the current densities were increased by 50-folds from 0.1 to 5 A g^{-1}, more than 50% of the theoretical capacity could be retained, demonstrating a respectable power capability. To estimate the superiority of current PTCDI for high-power cycling, we summarized the specific capacities in Figure 2c as a function of cycling currents among reported anodes in CIBs.[10] It clearly illustrates that PTCDI delivers the highest capacity retention of 70 mAh g^{-1} at an unprecedentedly high current density of 5 A g^{-1}. Figure 2d shows stable cyclic capacities of PTCDI at 0.2, 0.5, 1, 2 and 5 A g^{-1}. When the current density was turned back to 0.5 A g^{-1}, almost no capacity degradation was observed before and after the tough high-rate cycling processes. Figure 2e shows the cycling stability of PTCDI in extended 1000 cycles at 2 A g^{-1}, which manifests a high capacity retention of 80.3% equaling to an extremely low capacity fading rate of 0.02 % per cycle.

To explore the electrochemical kinetics for PTCDI anodes in ACIBs, CV profiles at different scan rates from 0.2 to 10 mV s^{-1} are exhibited in Figure 2f. The CV curves with distinctive redox peaks even scanning at 10 mV s^{-1} suggest rapid conversion kinetics for PTCDI anodes. The relationship between the peak current responses and the scan rates can be described by $i = av^b$, [18] where *v, i* and *a, b* refers to the scan rate, the current at a specific potential, and the adjustable parameters, respectively. In general, b =0.5 indicates a diffusion-controlled process, while a surface-controlled capacitive process dominates the reaction for b=1. **Figure S1** shows a linear relationship between log (v) and log (i) for the peak currents derived from Figure 2f. The b values were calculated to be 0.65 and 0.74 for anodic and cathodic peaks, respectively, rendering both capacitive- and diffusion-controlled processes for PTCDI anodes in ACIBs. The capacity contribution ratio at a certain scan rate can be quantitatively estimated

by fitting the capacitive regions.[19] It shows that at low scan rates (<1 mV s^{-1}), diffusion-controlled reaction dominated the Ca ion storage process, whereas the capacitive contribution played more significant roles at high scan rates (>1 mV s^{-1}, Figure 2g). In particular, the capacitive effect contributed 85.6% of the overall capacity at a high scan rate of 10 mV s^{-1} (**Figure S2**). Considering the micron-sized particles with long-range ordered crystal structure of PTCDI, the capacitive region can be denoted as the intercalation-pseudocapacitive behavior. It is beneficial to high-rate cycling through rapid surface and near-surface redox reactions.[19] In order to clarify the kinetics for the diffusion-controlled region, we calculated the Ca ion diffusion coefficients in PTCDI using galvanostatic intermittence titration technique (GITT) (**Figure S3**).[21] The diffusion coefficients associated with the calciation and decalciation processes are determined to be ranging from 10^{-8} to 10^{-10} cm^2 s^{-1}, which is superior to the Li^+ diffusion in $Li_4Ti_5O_{12}$ (10^{-11} to 10^{-12} cm^2 s^{-1})[22a] and Ca^{2+} migration in Ni-based metal-organic compounds (5.3×10^{-14} cm^2 s^{-1}).[22b] Overall, both the rapid ion migration kinetics and the surficial capacitive reactions contribute to the high-rate capability for PTCDI anodes in ACIBs.

In order to understand the Ca storage mechanisms in PTCDI anodes, we conducted combined theoretical and experimental investigations. Density functional theory (DFT) calculations were firstly performed to simulate the electronic feature and possible Ca^{2+} insertion sites in PTCDI. The band gap (E_g) between the lowest unoccupied molecular orbital (LUMO) and the highest occupied molecular orbital (HOMO) levels determines the electronic conductivity for organic compounds.[23] When the E_g value is lower than 2.5 eV, the electrode materials would indicate appreciable electronic conductivity.[24] The *E*g value for PTCDI is calculated to be 2.54 eV, proving its semiconductor nature (**Figure 3a**), which is superior to many insulating organic electrodes.[25] Figure 3b shows the simulated charge distributions for a single PTCDI molecule, where the red color regions stand for the positively charged perylene group and blue color region for the negatively charged carbonyl groups. The carbonyl motif (C=O) enables an *n*-type redox reaction accompanied by the formation of radical monoanion

(C-O$^-$) through enolization reaction, to be discussed in detail later. Electron could be coupled with the perylene core during calciation. The electronic and ionic accepting features lie the foundation for Ca insertion in PDCTI.

The structural evolution of PTCDI was measured by FTIR and Raman at different charge–discharge stages in the potential range of –1 to 0.2 V *vs.* Ag/AgCl. In the *ex-situ* FTIR spectra (Figure 3c), the peak intensity of carbonyl group located at 1676 cm^{-1} became gradually weaken upon calciation, which is associated with the appearance of a new peak at 1635 cm^{-1} referring to the chemical bonding of Ca^{2+} and –COO^-. This result suggests the conversion of carbonyl group (C=O) to enolizated C-O$^-$ during calciation. Upon decalciation, the peak for carbonyl groups was entirely recovered, indicating the highly reversible (de)enolization reactions of PTCDI in ACIBs. Different from intercalation- or alloying-type anodes involving solid-state-ion diffusion, the enolization reaction without covalent bond cleavage or reformation favors high-power cycling. To clarify whether Ca ions are intercalated in the stacked aromatic carbon rings of PTCDI, *in-situ* Raman measurement (Figure 3d) was conducted. The graphene-like perylene layers in PTCDI claimed D band (1352 cm^{-1}, referring to perylene ring stretching) and G band (1606 cm^{-1}, referring to perylene ring stretching) Raman peaks.[26] Interestingly, no peak shift was observed during the whole discharging and charging processes. Therefore, it is the enolization of carbonyl groups instead of intercalation in perylene layers contributing the Ca^{2+} ion storage capacities to PDCTI.

The successful accommodation of Ca^{2+} in PDCTI was further claimed by X-ray photoelectron spectrometry (XPS) and ^{13}C NMR characterizations. Figure 3e shows the XPS spectra of Ca 2*p* before and after calciation of PTCDI. Two strong peaks at 351.3 and 347.8 eV corresponding to the Ca-2$p_{1/2}$ and Ca-2$p_{3/2}$ are clearly observed after calciation. Negligible Ca 2*p* peaks was observed for decalciated PTCDI. Simultaneously, the deconvoluted XPS spectra of O1*s* in Figure 3f show reversible shift between 532.6 eV to 531.9 eV, corresponding to the C=O and C-O$^-$ groups, respectively, once again verifying the reversibility of enolization

reactions. A deeper insight into the structural evolution of active sites in PTCDI was revealed by ^{13}C solid-state NMR (Figure 3g). The resonance peaks at 100–140, 161.6, and 165.2 ppm are assigned to the perylene and carbonyl carbons in pristine PTCDI. [27] After calciation, the peaks for carbonyl group merged into a broadened peak at 166.9 ppm due to the blended electronic environment around mono-anion after enolization. The peaks at 120.9 and 132.7 ppm assigned to aromatic rings are broadened with a new resonance peak at 109.7 ppm. These results suggest electronic shielding among the aromatic carbon ring after calciation. The peaks of aromatic rings and carbonyl groups were recovered after decalciation, highlighting the structural reversibility of PTCDI. The new peak at 146.2 ppm may be attributed to the nonuniformity of the decalciated samples with unpaired electrons in the organic ligands. [27] The successful calciation of PTCDI was also claimed by electron energy-loss spectroscopy (EELS) curve in **Figure S4**.

To unveil the nature of charge carriers in PTCDI, *in-situ* electrochemical quartz crystal microbalance (EQCM) measurement was carried out by CV scanning at 1 mV s^{-1} (**Figure 4a**). During the cathodic scan down to −0.7 V *vs*. Ag/AgCl, the electrode experienced a rapid mass gain because of cation insertion. A mass loss is clearly observed as further scanning to -1.0 V. Similar phenomenon was also observed in H_3O^+ intercalation in MoO_3 electrodes in aqueous cells, which was interpreted as water exaction from solvated cation intercalants. [28] Analogically, we speculated that $[H_2O\text{-}Ca]^{2+}$ co-insertion may partially occur due to the strong desolvation energies for divalent Ca^{2+}. More efforts will be performed to illustrate the origin of the abnormal mass loss in future works. In the anodic scan, the mass change is reversible to the cathodic sweep. In the potential range of −0.25 to −0.5 V, a rapid mass loss can be ascribed to the exaction of Ca^{2+}. At 0.2 V, the electrode mass is completely reversed back to its original stage, demonstrating the reversible Ca^{2+} insertion/extraction in PTCDI.

Having verified the Ca^{2+} storage in PTCDI through enolization reactions, we then attempted to unveil the Ca^{2+} migration pathway through *ex-situ* XRD characterization (Figure

4b and **Figure S5**). The peaks at 12.1°, 25.3°, 27.2°, and 38.6° are indexed to (020), (11$\bar{2}$), (12$\bar{2}$), and (114) planes of pristine PTCDI. As the Ca^{2+} ions inserted and migrated in PTCDI, a slightly positive shift of the (020) peak position was observed. Coincidently, carbonyl groups in PTCDI line up along the (020) plane as shown in **Figure S6**. Given the aligned and packed wave-layer crystals, the only feasible Ca ion migration tunnel is along the *a* axis (perpendicular to the (020) plane). Variations of the lattice parameters occur during Ca insertion and extraction along this pathway. **Figure S7** and **Table S3** show the Retiveld refinement XRD information of the fully discharged PTCDI samples. During calciation, the peaks of (020) and (114) shifted to higher angles by 0.2°, rendering a contraction in the *b* axis from 14.76762 to 14.70084 Å. The blue shift of (11 $\bar{2}$) and (12 $\bar{2}$) planes indicate the expansion in *a/c* planes from 4.88651/10.90941 Å to 4.92062/11.05861 Å, respectively. The contradictive variation of lattice parameters induces an extremely low volume change of 1.6% for PTCDI upon calciation. Moreover, the high-degree crystallinity was retained as shown by the strong intensity of all diffraction peaks during cycling. The intact 3D framework and no dissolution for PTCDI demonstrated their integrity in ACIBs. After decalciation, all peaks recovered, consistent with above XPS, ^{13}C NMR and EQCM results.

Based on the above experiments and calculations, we can schematically illustrate the Ca^{2+} insertion sites and diffusion pathway in Figure 4c. During calciation, Ca^{2+} ions migrate along the (002) plane to enolize carbonyl groups. This results in the elongation of the (11$\bar{2}$) and (12$\bar{2}$) planes and contraction of (020) and (114) planes. The one-dimensional Ca^{2+} ion diffusion tunnel along the *a* axis is responsible to the high capacity utilization and the high-power capability. In addition, the Ca^{2+} would not penetrate through the aromatic carbon layers as evidenced by the intact D- and G-band shift in the Raman spectra (Figure 3d**)**. In-plane migration of Ca^{2+} ions among carbon layers was demonstrated thermodynamically and kinetically unfavorable.[29] Absence of this adverse Ca^{2+} diffusion pathway is in turn beneficial

for high-power cycling PTCDI. No dissolution of active materials is also important for long-term cycling of PTCDI in aqueous electrolyte. Marginal changes were observed for the calciated and decalciated PTCDI particles as shown in morphological characterization results (Figure 4d, 4e and **Figure S8)**. Overall, PTCDI is an appealing anode undergoing rapid Ca storage capability with superior structural stability in ACIBs.

Finally, to verify the practical feasibility of PTCDI anodes, we built high-power ACIB prototypes using a copper-based Prussian blue analogous (Cu-PBA) cathode and 1M $CaCl_2$ aqueous electrolyte. The XRD diffraction peaks of Cu-PBA (**Figure 5a**) were indexed to a face-centered cubic lattice with a space group of $Fm3^{-}m$. Figure 5b shows the morphology of Cu-PBA with uniform particles of ~50 nm in size. The electrochemical property of Cu-PBA was examined by cycling at 0.1 A g^{-1} in 1 M $CaCl_2$ aqueous solution using a three-electrode setup. The first five cycles' charge–discharge voltage profiles in Figure 5c show excellent reversibility and high capacities of 62 mAh g^{-1}. The Cu-PBA cathode was fully calciated before assembling with PTCDA into CIB full cells. Figure 5d shows the galvanostatic discharge–charge profiles of PTCDA//Ca-Cu-PBA full cells cycled between 0–1.8 V. It shows discharge capacities of 147.7, 117.2, 87.1, and 55.9 mAh g^{-1} at 0.1, 0.2, 0.5, and 1 A g^{-1}, respectively. Correspondingly, at a specific high power of 1000 W kg^{-1}, a high specific energy of 64.5 Wh kg^{-1} could be achieved based on the mass loading of PTCDI. Figure 5e exhibits the excellent cyclability of the full cells at 1 A g^{-1} with a capacity retention of 87.2 % over 200 cycles. The nonflammable ACIBs using green organic electrodes feature low-cost, non-toxic, and easily mass-producing, which are primarily considered indicators for grid-scale energy storage applications.

3. Conclusions

In summary, we reported an organic small molecular crystal PTCDI as high-power and long-cycle calcium storage anodes in ACIBs for the first time. The carbonyl group enolization redox chemistry and one-dimensional diffusion pathways hold the keys to

unlock the high-rate and reversible Ca^{2+} storage in PTCDI. In specific, an unprecedentedly low capacity degradation rate of 0.02 % per cycle over 1000 cycles was demonstrated by the high-capacity PTCDI anodes. The Ca^{2+} insertion mechanisms and the origins of the high-power capability were elucidated by a suit of comprehensive characterizations including *in-situ* Raman, XRD, and EQCM. This work successfully nudges the reversible Ca^{2+} storage in organic small organic molecules in aqueous system, which provides an unexplored pathway toward constructing sustainable and safe organic CIBs.

4. Experimental section

Material synthesis and characterizations. PTCDI was purchased and used without further purification. Cu-PBA nanoparticles were synthesized by a co-precipitation method. [14b] Typically, 0.1 M $Cu(NO_3)_2$ and 0.05 M $K_3Fe(CN)_6$ aqueous solutions (10 mL) were simultaneously (~0.11 mL min^{-1}) added into 60 mL deionized water drop by drop under vigorous stirring. After the sonication of the brown precipitate, the suspension was filtered and washed with deionized water. Samples were then dried in air at 80 °C for 48 hours.

The XRD tests were conducted on a Rigaku SmartLab 9kW diffractometer with Cu-Kα radiation. The Rietveld refinement was conducted through the GSAS program.[30] The XPS test was conducted on a Thermo Escalab 250Xi photoelectron spectrometer to evaluate the chemical structures. The morphologies and microstructures were examined by a Hitachi S-4800 field emission SEM and a JEOL JEM-2100F TEM. The chemical structure and functional groups were identified by Nicolet IS10 FTIR spectrometer, WITEC Alpha300 confocal Raman microscopy, and JEOL JNM600R, ^{13}C NMR spectrometer.

Electrochemical characterizations. The anode electrodes were prepared by pressing a paste made by mixing PTCDI powder, Super-P carbon, and polytetrafluoroethylene in a weight ratio of 6:3:1 on the titanium mesh current collectors followed by drying at 80 °C. The active mass

loading was ~2 mg cm^{-2}. The Cu-PBA cathode electrodes were prepared in the same way as PTCDI anode with a weight ratio 8:1:1 for active material: super P: binder. The electrochemical performance on the electrodes was performed in the three-electrode configurations with Pt as the counter electrode, Ag/AgCl as the reference electrode, and 1 M $CaCl_2 \cdot 2H_2O$ aqueous electrolyte. The galvanostatic charge–discharge profiles and the GITT experiments were performed by using a Neware CT-3008 battery tester. The CV curves were measured on a CHI 660e electrochemical workstation.

Electrochemical quartz crystal microbalanc (EQCM) tests were carried out on SRS QCM200 quartz crystal microbalance. The PTCDI-based slurry was sprayed on a 1-in. quartz crystal disk. The weight change of electrode materials was measured during CV scanning at 1 mV s^{-1}, while a mass change (Δm) of the electrode coated on the quartz crystal was converted from the frequency change of the quartz resonator (Δf) by the Sauerbrey's equation. $\Delta m = \frac{\sqrt{\rho_q \mu_q}}{2 f_0} * \Delta f$, where ρ_q, μ_q, and f_0 stand for the density of quartz, the shear modulus of quartz, and the fundamental resonance frequency of the quartz, respectively.

Calculations. The DFT calculations were optimized based on a B3LYP molecular geometry with the 6-31G* on a basis set using the Gaussian program suite.[31] The LUMO and HOMO levels for the PTCDI molecule were plotted by the Multiwfn program.[32] The electrostatic potential maps and optimized molecular structures for PTCDI are generated by the VMD program.[33]

Supporting Information

Supporting Information is available from the Wiley Online Library or from the author.

Acknowledgements

This work described in this paper was fully supported by grants from the Research Grants Council of the Hong Kong Special Administrative Region, China (Project No. PolyU25216121, PolyU15305022) and the Research Committee of the Hong Kong Polytechnic University under project codes A-PB1M, 1-BE3M, 1-CD4M, 1-BBR0, and

RHUP. We acknowledge the TEM characterization assistance from Ye Zhu's group at PolyU.

Received: ((will be filled in by the editorial staff))
Revised: ((will be filled in by the editorial staff))
Published online: ((will be filled in by the editorial staff))

References

[1] a) M. Armand, J.-M. Tarascon, *Nature* **2008**, *451*, 652; b) B. Dunn, H. Kamath, J. M. Tarascon, *Science* **2011**, *334*, 928. c) D. L. Wood Iii, J. Li, C. Daniel, *J. Power Sources* **2015**, *275*, 234; d) P. Canepa, G. Sai Gautam, D. C. Hannah, R. Malik, M. Liu, K. G. Gallagher, K. A. Persson, G. Ceder, *Chem. Rev.* **2017**, *117*, 4287.

[2] a) H. D. Yoo, I. Shterenberg, Y. Gofer, G. Gershinsky, N. Pour, D. Aurbach, *Energy Environ. Sci.* **2013**, *6*, 2265; b) R. Schmuch, R. Wagner, G. Hörpel, T. Placke, M. Winter, *Nat. Energy* **2018**, *3*, 267; c) J. Muldoon, C. B. Bucur, T. Gregory, *Chem. Rev.* **2014**, *114*, 11683; d) D. Aurbach, Z. Lu, A. Schechter, Y. Gofer, H. Gizbar, R. Turgeman, Y. Cohen, M. Moshkovich, E. Levi, *Nature* **2000**, *407*, 724.

[3] a) X. Sun, V. Duffort, L. F. Nazar, *Adv. Sci.* **2016**, *3*, 1600044; b) L. Stievano, I. D. Meatza, J. Bitenc, C. Cavallo, S. Brutti, M. A. Navarra, *J. Power Source* **2021**, *482*, 22875.

[4] G. V. Lewis, C. R. A. Catlow, *J. Phys. C: Solid State Phys.* **1985**, *18*, 1149.

[5] J. Muldoon, C.B. Bucur, A.G. Oliver, T. Sugimoto, M. Matsui, H.S. Kim, G.D. Allred, J. Zajicek, Y. Kotani, *Energy Environ. Sci.* **2012**, *5*, 5941.

[6] R. J. Gummow, G. Vamvounis, M. B. Kannan, Y. He, *Adv. Mater.* **2018**, *30*, 1801702.

[7] H. W. Song, C. X. Wang, *Adv. Energy Sustainability Res*. **2022**, *3*, 2100192.

[8] a) L. Stievano, I. D. Meatza, J. Bitenc, C. Cavallo, S. Brutti, M. A. Navarra, *J. Power Sources* **2021**, *482*, 228875. b) A. M. Melemed, A. Khurram, B. A. Gallant, *Batteries & Supercaps* **2020**, *3*, 570.

[9] a) J. Park, Z. L. Xu, G. Yoon, S. K. Park, J. Wang, H. Hyun, H. Park, J. Lim, Y. J. Ko, Y. S. Yun, K. Kang, *Adv. Mater.* **2020**, *32*, 19004411; b) N. Wu, W. Yao, X. Song, G. Zhang, B. Chen, J. Yang, Y. Tang, *Adv. Energy Mater.* **2019**, *9*, 1803865; c) M. Wang, C. Jiang, S. Zhang, X. Song, Y. Tang, H.-M. Cheng, *Nat. Chem.* **2018**, *10*, 667.

[10] M. E. A. Dmpablo, A. Ponrouch, P. Johansson, M. R. Palacín, *Chem. Rev.* **2020**, *120*, 6331.

[11] C. Chen, F. Shi, Z.-L. Xu, *J. Mater. Chem. A* **2021**, *9*, 11908.

[12] S. Muench, A. Wild, C. Friebe, B. Haupler, T. Janoschka, U.S. Schubert, *Chem. Rev.* **2016**, *116*, 9438.

[13] Z. Song, Y. Qian, M. Otani, H. Zhou, *Adv. Energy Mate*r. **2016**, *6*, 1501780.

[14] a) C. Han, H. Li, Y. Li, J. Zhu, C. Zhi, *Nature Commun.* **2021**, *12*, 2400; b) S. Gheytani, Y. Liang, F. Wu, Y. Jing, H. Dong, K. K. Rao, X. Chi, F. Fang, Y. Yao, *Adv. Science* **2017**, *4*, 1700465; c) M. S. Chae, A. Nimkar, N. Shpigel, Y. Goger, D. Aurbach, *ACS Energy Lett.* **2021**, *6*, 2659; d) S. Q. Zhang, Y. L. Zhu, D. H. Wang, C. G. Li, Y. Han, Z. Shi, S. H. Feng, *Adv. Sci.* **2022**, *9*, 2200397.

[15] C.L. Wang, H.L. Dong, L. Jiang, W.P. Hu, *Chem. Soc. Rev.* **2018**, *47*, 422.

[16] O. Mizrahi, N. Amir, E. Pollak, O. Chusid, V. Marks, H. Gottlieb, L. Larush, E. Zinigrad, D. Aurbach, *J. Electrochem. Soc.* **2008**, *155*, A103.

[17] X. Wang, C. Bommier, Z. Jian, Z. Li, R. S. Chandrabose, I. A. R. Perez, P. A. Greaey, X. Ji, *Angew. Chem. Int. Ed.* **2017**, *56*, 2909.

[18] V. Augustyn, J. Come, M. A. Lowe, J. W. Kim, P. L. Taberna, S. H. Tolbert, H. D. Abruna, P. Simon, B. Dunn, *Nature Matter.* **2013**, *12*, 518.

[19] R. J. Li, X. Z. Zhu, Q. F. Fu, G. S. Liang, Y. J. Chen, L. J. Luo, M. Y. Dong, Q. Shao, C. F. Lin, R. B. Wei, Z. H. Guo, *Chem. Commun.* **2019**, *55*, 2493.
[20] V. Augustyn, P. Simon, B. Dunn, *Energy Environ. Sci.* **2014**, *7*, 1597.
[21] K. Tang, X. Yu, J. Sun, H. Li, X. Huang, *Electrochim. Acta*, **2011**, *56*, 4869.
[22] Y. H. Rho, K. Kanamura, *J. Solid State Chem.* **2004**, *177*, 2094; b) V. N. Vo, J. Hur, I. T. Kim, *ACS Sustain. Chem.* **2020**, *8*, 2596.
[23] A. Ajayaghosh, *Chem. Soc. Rev.* **2003**, *32*, 181.
[24] G. Zotti, S. Zecchin, G. Schiavon G, L. Groenendaal, *Chem. Mater.* **2000**, *12*, 2996.
[25] Y. Lu, J. Chen, *Nat. Rev. Chem.* **2020**, *4*, 127.
[26] L. P. Yang, P. Y. Wang, S. W. Zhang, Y. H. Wang, L. Zang, H. Zhu, J. Yin, H. Y. Yang, *J. Mater. Chem. A* **2020**, *8*, 22791.
[27] Y. Liu, X. Zhao, C. Fang, Z. Ye, Y. He, D. Lei, J. Yang, Y. Zhang, Y. Li, Q. Liu, Y. Huang, R. Zeng, L. Kang, J. Liu, Y.-H. Huang, *Chem* **2018**, *4*, 1.
[28] H. Jiang, W. Shin, L. Ma, J. J. Hong, Z. X. Wei, Y. S. Liu, S. Y. Zhang, X. Y. Wu, Y. K. Xu, Q. B. Guo, M. A. Subramanian, W. F. Stickle, T. P. Wu, J. Lu, X. L. Ji, *Adv. Energy Mater.* **2020**, *10*, 2000968.
[29] a) S. Thinius, M. M. Islam, P. Heitjans, T. Bredow, *J. Phys. Chem. C* **2014**, *118*, 2273; b) I. Abate, C. D. Pemmaraju, S. Y. Kim, K. H. Hsu, S. Sainio, B. Moritz, J. Vinson, M. F. Toney, W.L. Yang, W. E. Gent, T. P. Devereaux, L. F. Nazar, W. C. Chueh, *Energy Environ. Sci.* **2021**, *14*, 4858.
[30] a) B. H. Toby, *J. Appl. Crystallogr.* **2001**, *34*, 210; b) A.C. Larson, R.B. Von Dreele, LosAlamos National Laboratory Report LAUR **1994**, 86.
[31] Frisch, M. J.; Trucks, G. W.; Schlegel, H. B.; Scuseria, G. E.; Robb, M. A.; Cheeseman, J. R.; Scalmani, G.; Barone, V.; Petersson, G. A.; Nakatsuji, H. et al. Gaussian 09, Revision D.01; Gaussian, Inc.: Wallingford, 2009.
[32] Lu, T.; Chen, F. W. Multiwfn: *J. Comput. Chem.* 2012, 33, 580–592.
[33] Humphrey, W.; Dalke, A.; Schulten, K. *J. Mol. Graph.* 1996, 14, 33–38.

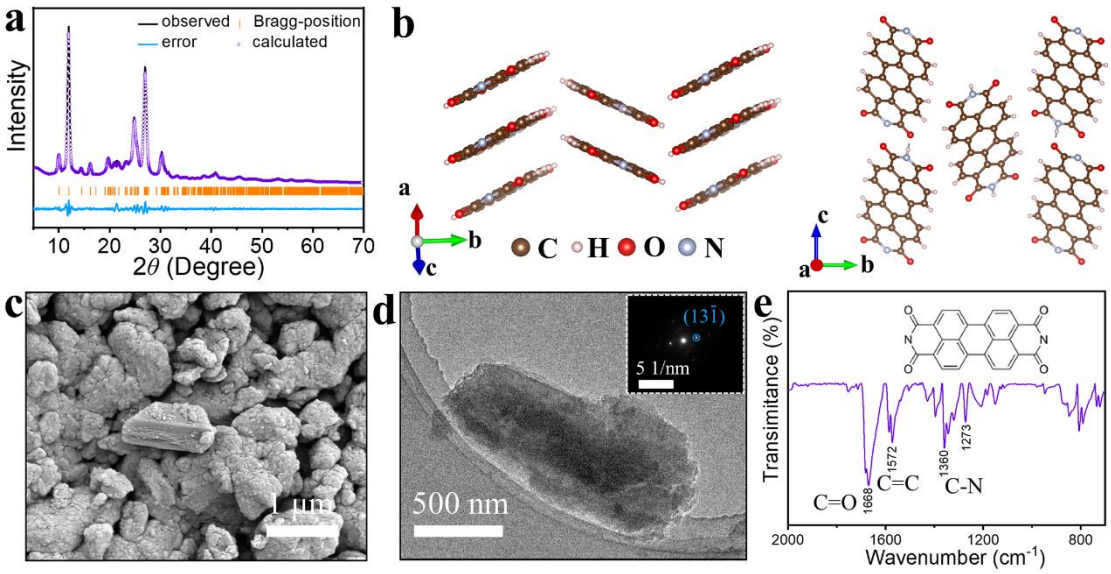

Figure 1. (a) XRD pattern with Rietveld refinement of PTCDI. (b) Schematic illustration of PTCDI molecular crystal. (c) SEM image, (d) TEM image with SAED pattern, and (e) FTIR spectrum for PTCDI electrode material.

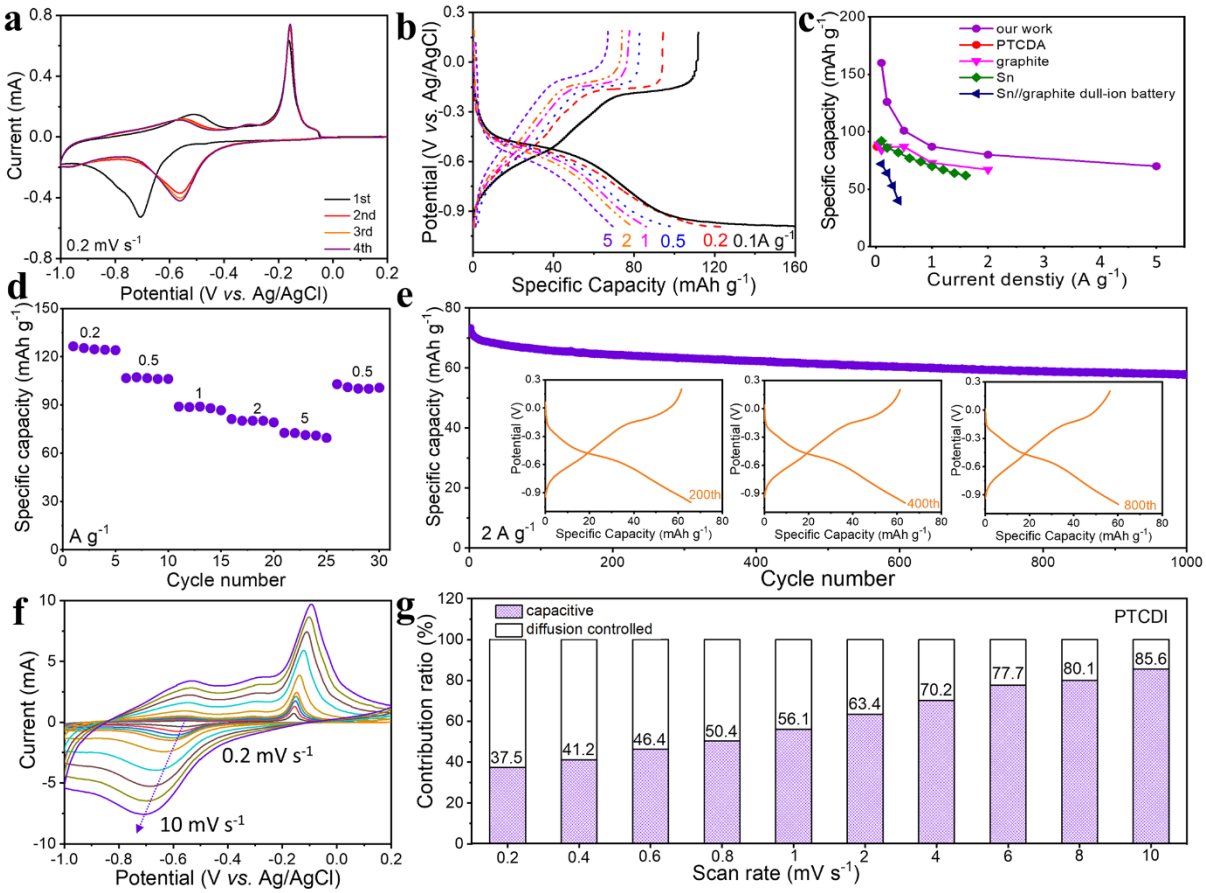

Figure 2. (a) First four-cycle CV curves for PTCDI at 0.2 mV s^{-1}. (b) Charge–discharge curves of PTCDI at different current rates. (c) Rate capacities of PTCDI in this work compared with other anode materials reported in literature. [9, 14c] (d) Cyclic capacities of PTCDI at current densities from 0.2 to 5 A g^{-1}. (e) Cycling stability of PTCDI at 2 A g^{-1} over 1000 cycles. (f) CV curves of PTCDI at scan rates from 0.2 to 10 mV s^{-1}, and (g) percentages of capacitive- and diffusion-controlled capacity contributions of PTCDI under increasing scan rates.

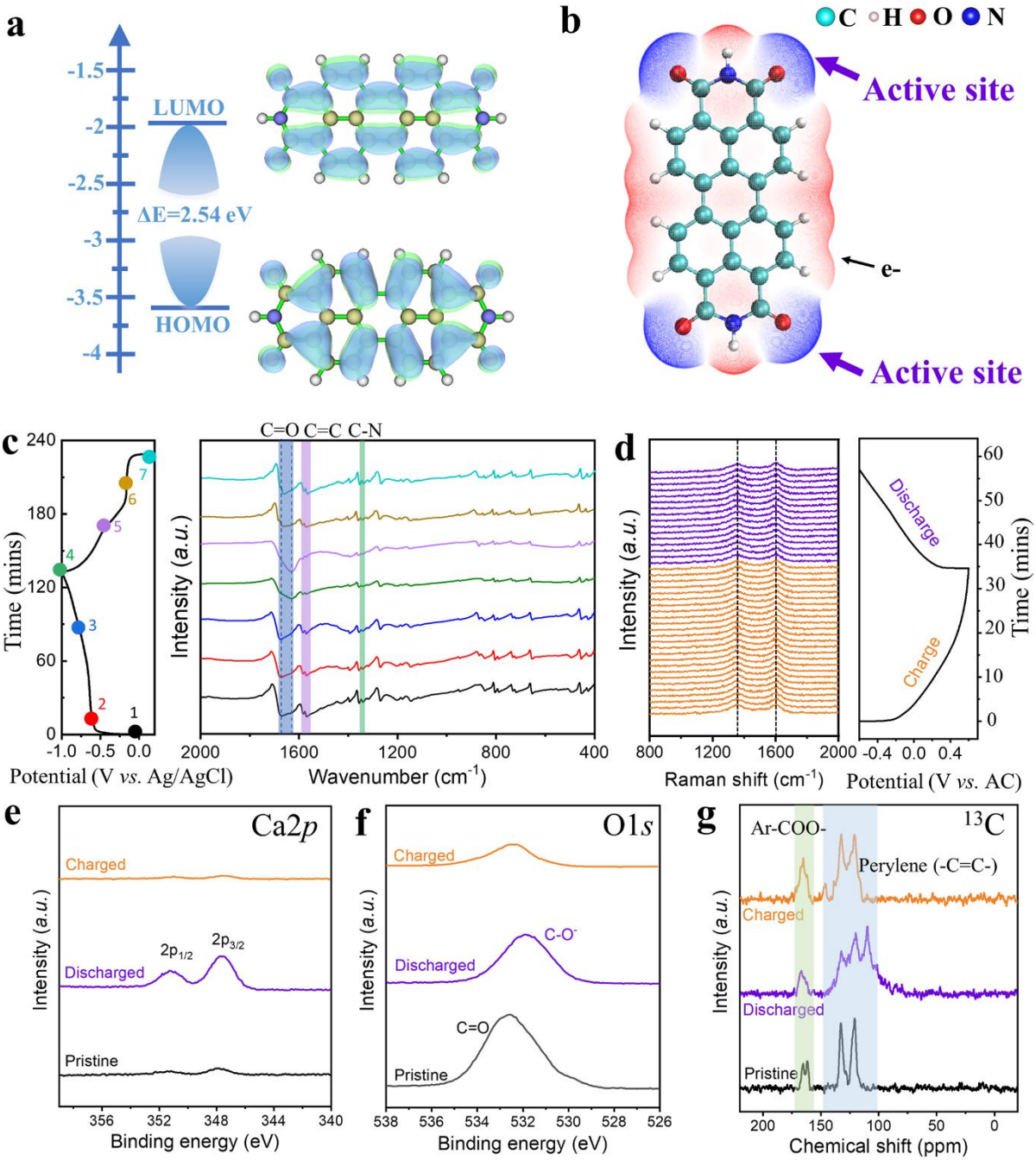

Figure 3. (a) Calculated HOMO and LUMO levels of PTCDI. (b) Charge distribution visualization of PTCDI. (Color profile: blue for the negative charge and red for the positive charge) (c) *Ex-situ* FTIR spectra of PTCDI and the corresponding charge–discharge profile. (d) *In-situ* Raman spectra of PTCDI. (e) XPS Ca 2*p*, (f) XPS O 1*s*, and (g) ^{13}C solid-state NMR spectra of pristine (down), discharged (middle) and charged (up) PTCDI in ACIBs.

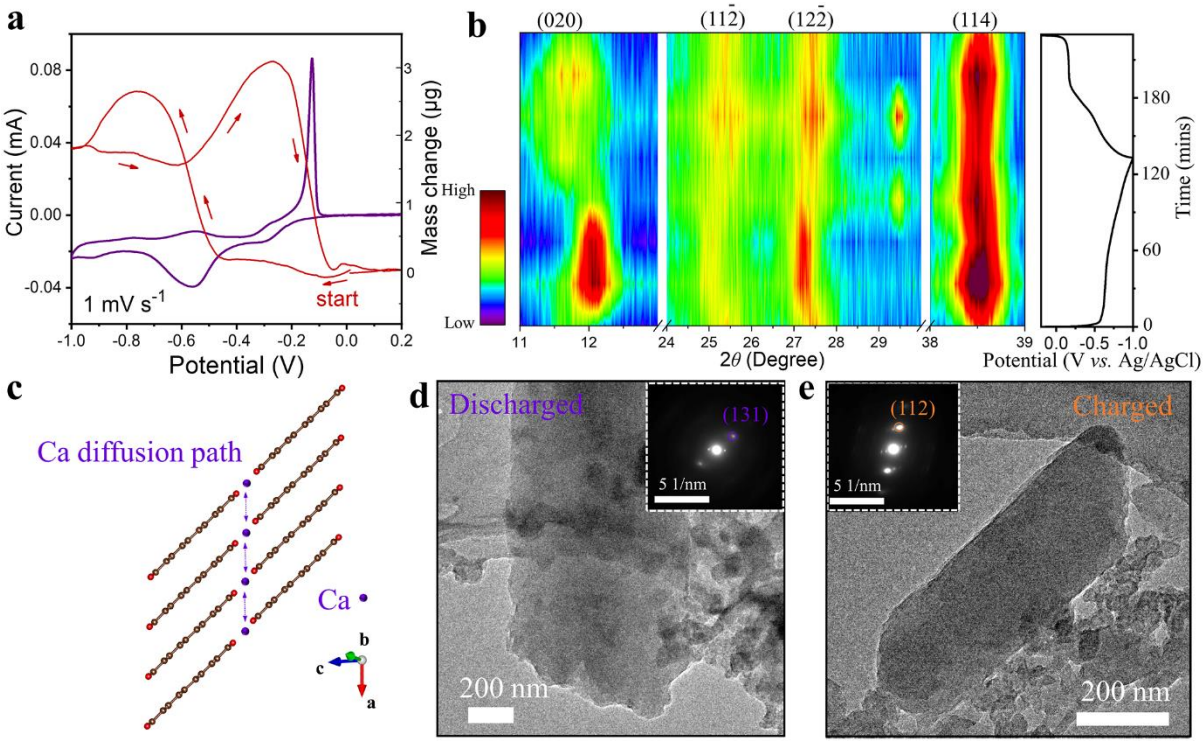

Figure 4. (a) EQCM profile of PTCDI at a CV scanning rate of 0.2 mV s^{-1}. (b) *Ex-situ* XRD patterns and the corresponding charge–discharge profile. (c) Schematic image of the calcium ion diffusion pathway. TEM images and SAED patterns of (d) discharged and (e) charged PTCDI.

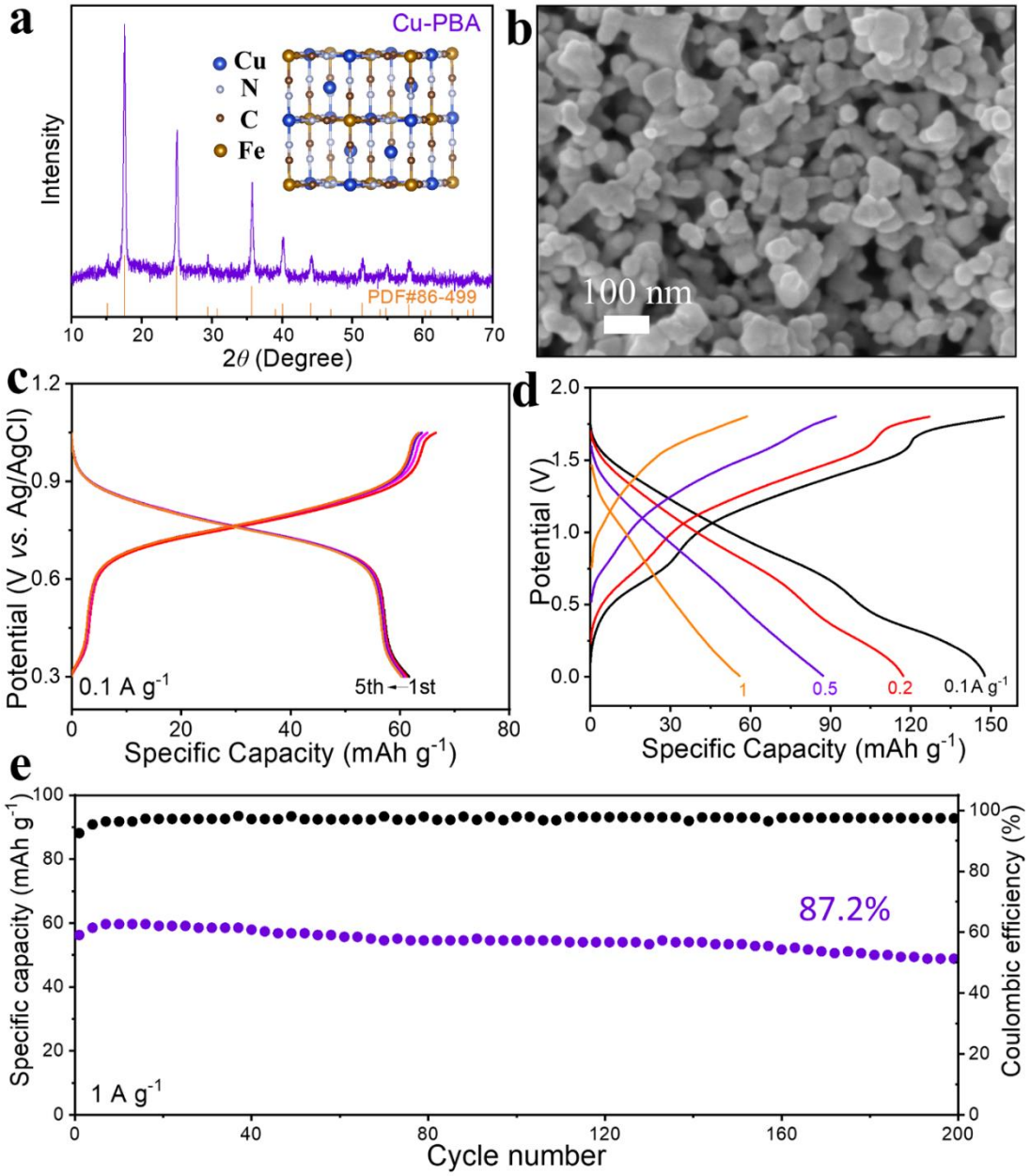

Figure 5. (a) XRD pattern and illustrated crystal structure of Cu-PBA. (b) SEM image of Cu-PBA nanoparticles. (c) Charge–discharge curves of Cu-PBA at 0.1 A g^{-1}. (d) Charge–discharge curves at different current densities, and (e) the cyclic capacities and coulombic efficiencies of PTCDI//Ca-Cu-PBA full cells.

PTCDI is first employed as the anode for aqueous calcium-ion batteries. The guest-host chemical bonding and structure evolution of molecular crystals are clearly clarified by simulation and *in(ex)-situ* spectroscopy characterizations. This study extends the boundary of molecular crystal systems for electrochemistry to construct high-performance aqueous multivalent ion batteries.

*Renjie Li, Jingya Yu, Feiyang Chen, K.C. Chan, Zheng-Long Xu**

High-power and ultrastable aqueous calcium-ion batteries enabled by small organic molecular crystal anodes